Semi-solid Constitutive Parameters and Failure Behavior of a Cast AA7050 Alloy

Subroto, Tungky; Eskin, Dmitry G.; Miroux, Alexis; Ellingsen, Kjerstin; M'Hamdi, Mohammed; Katgerman, Laurens

DOI
10.1007/s11661-020-06112-5

Publication date
2021

Document Version
Final published version

Published in
Metallurgical and Materials Transactions A: Physical Metallurgy and Materials Science

Citation (APA)
Subroto, T., Eskin, D. G., Miroux, A., Ellingsen, K., M'Hamdi, M., & Katgerman, L. (2021). Semi-solid Constitutive Parameters and Failure Behavior of a Cast AA7050 Alloy. *Metallurgical and Materials Transactions A: Physical Metallurgy and Materials Science*, *52*(2), 871-888. https://doi.org/10.1007/s11661-020-06112-5

ORIGINAL RESEARCH ARTICLE

Semi-solid Constitutive Parameters and Failure Behavior of a Cast AA7050 Alloy

TUNGKY SUBROTO, DMITRY G. ESKIN, ALEXIS MIROUX, KJERSTIN ELLINGSEN, MOHAMMED M'HAMDI, and LAURENS KATGERMAN

AA7050 is an aluminum alloy with superior mechanical properties; however, it is prone to hot tearing (HT) during its production via direct-chill casting. This study focuses on extracting constitutive parameters of the alloy thermomechanical behavior in semi-solid state as well as gaining insight in its failure behavior. Tensile tests were performed using an Instron 5944 at solid fractions between 0.85 (550 °C) and 1.0 (465 °C), at deformation rates of 0.2 and 2 mm/min. The results showed that there are three mechanical behavior regimes in this solid fraction range: ductile at 1.0 (T = 465 °C) ≤ f_s < 0.97 (T = 473 °C), brittle at 0.97 (T = 473 °C) ≤ f_s ≤ 0.9 (T = 485 °C) and then ductile again (at 0.9 (T = 485 °C) < f_s ≤ 0.85 (T = 550 °C)). Fracture surface analysis revealed that the fracture mode was mostly intergranular with fracture propagating through solid bridges as well. Semi-solid constitutive parameters were obtained by making a simple thermal model and numerical tensile tests in ALSIM software package and comparing the simulation results with experimental mechanical tests. The extracted constitutive parameters and available information from the literature support the fact that AA7050 is more susceptible to HT than AA5182 and Al-2 wt pct Cu alloys. The obtained parameters can further enhance the predictive capability of computer simulations of direct-chill casting.

https://doi.org/10.1007/s11661-020-06112-5

I. INTRODUCTION

AA7XXX-SERIES aluminum alloys are critical for structural applications in aerospace industries because of their superior mechanical properties, such as high strength and enhanced fracture toughness.[1,2] One major route to produce this type of alloys for further downstream processing is through direct-chill casting (DC casting).[3]

Although DC casting is a robust production method and able to meet industrial standards, the nature of the process introduces severe thermal gradients in a cast ingot during casting. The shell of the ingot that has just solidified comes in direct contact with cooling water, while the center of the ingot is still partially liquid or, in larger ingots, may be still in the fully liquid state. These thermal gradients in connection with greatly different mechanical behavior of the different sections of the ingot augment the formation of casting defects, in particular hot tear (HT) and cold crack (CC).

HT is one of the critical solidification defects that may form during casting. It occurs when the alloy is at its semi-solid state, especially towards the end of solidification (below the rigidity temperature when the dendrites have connected to each other and the alloy has gained some mechanical strength) where there is no sufficient melt to feed the shrinkage, which under imposed thermal stresses may result in crack formation in the billet. HT has different levels of severity, starting from micro-scale HT, which can be healed through further processing, *i.e.,* hot-isostatic-pressing,[4] up to the catastrophic level where the solidified billet cannot be used for subsequent processing and rendered useless. In any case, the presence of HT in the billet will reduce the quality of the cast product and increase the production cost of the alloy, and thus needs to be minimized.

TUNGKY SUBROTO is with the Materials innovation institute (M2i), Mekelweg 2, 2628 CD Delft, The Netherlands and also with the Department of Materials Science and Engineering, Delft University of Technology, Mekelweg 2, 2628 CD Delft, The Netherlands and also with the BCAST, Brunel University London, Uxbridge, Middlesex, UB8 3PH, UK. Contact e-mails: Tungky.subroto@gmail.com; Tungky.subroto@brunel.ac.uk DMITRY G. ESKIN is with the BCAST, Brunel University London and also with the Tomsk State University, Tomsk, Russia 634050. ALEXIS MIROUX is with the Materials innovation institute (M2i) and also with the Department of Materials Science and Engineering, Delft University of Technology and also with the Alvance Aluminium Duffel, 2570 Duffel, Belgium. KJERSTIN ELLINGSEN is with the SINTEF Materials and Chemistry, 0314 Oslo, Norway. MOHAMMED M'HAMDI is with the SINTEF Materials and Chemistry and also with Department of Materials Science and Engineering, Norwegian University of Science and Technology, 7491 Trondheim, Norway. LAURENS KATGERMAN is with the Department of Materials Science and Engineering, Delft University of Technology.

Manuscript submitted June 16, 2020; accepted November 23, 2020.
Article published online January 8, 2021

HT formation has been extensively studied and reviewed; see Reference 5 for the conditions and mechanisms of HT formation and Reference 6 for the properties of semi-solid alloys, which are directly linked to the HT phenomenon. Susceptibility of the alloy to HT depends on both microscopic and macroscopic features of the alloy. Grain size (including secondary dendrite arms spacing)[7] and the presence of harmful intermetallics in the structure[8] may affect the HT susceptibility. Meanwhile, the chemical composition[9] affects the semi-solid mechanical behavior of the alloy[6,10–12] through the phase composition but also through the freezing range of the alloy[6,9]—the wider, the more susceptible to HT. However, it is also understood that the longer the portion of the solidification part where melt feeding is insufficient compared to the part of the solidification range where feeding is still active, the more the alloy is prone to HT.[13] The uneven cooling conditions in the ingot due to the nature of the DC casting process result in tensile thermal stresses imposed on the part of the billet which is still in the semi-solid state. This, combined with insufficient melt feeding to the formed dendritic network, may lead to the formation of HT.[11,12] Therefore, to better understand the HT susceptibility of an alloy, it is crucial to take into account the onset thermal contraction temperature (determining the beginning of the temperature range vulnerable to HT) as well as the total amount of thermal contraction (correlated to the strain imposed on the semi-solid material). An AA7050 alloy has a relatively long freezing range,[14] and the thermal contraction starts at a relatively low solid fraction compared to other alloys.[15–17] Combined with DC casting conditions that aggravate the thermomechanical condition in the solidifying ingot, it can be inferred that producing a quality AA7050 billet through DC casting is difficult because of its propensity to HT occurrence. Additionally, an AA7050 alloy demonstrates large thermal expansion and low thermal conductivity, which implies that large thermal residual stress could be generated during cooling, and ultimately makes this alloy prone to CC. Since catastrophic CC may be initiated through micro-scale HT acting as pre-existing cracks,[18] the formation of HT is intimately related to CC. A careful selection of process conditions to produce sound AA7050 billets without HT and CC needs to be done. This is because CC not only reduces the productivity of a manufacturing company but also poses safety hazard for the casting personnel and hardware, and thus needs to be minimized.

For decades, the R&D efforts were focused on minimizing the HT occurrence during DC casting (without changing the alloy compositions). Those included finding the best casting temperature[19] and trying various melt flow schemes to feed the liquid pool.[20] It was also clear that reducing the casting speed was the most effective way to reduce HT.[9] However, reducing casting speed implies lowering the production rate, and hence the profitability of the company. Thus, an optimum casting speed has to be found to maximize the casting performance and quality. Traditionally, this is done by trial and error. However, with the advent of powerful computers, numerical process optimization is the preferable course of action as it saves both time and resources.

In this work, we used ALSIM, a numerical model enabling us to simulate aluminum casting processes. This package includes an advanced solidification model which accounts for solidification defects such as HT and CC.[21,22] To simulate the casting process accurately, this model needs a set of constitutive parameters which are unique for different alloys. Such parameters are typically obtained by fitting a set of model parameters to the experimental data. At the moment, ALSIM only has constitutive parameters for an AA7050 alloy in the fully solid state[23] and the sub-solidus regime.[24] Hence, ALSIM is currently lacking a constitutive behavior database for the semi-solid regime of an AA7050 alloy,[20] needed for modeling HT behavior. Instead, the Al-2 wt pct Cu data are used to complete the semi-solid part of the database. However, thermophysical properties of these two alloys are different (*e.g.*, freezing range of AA7050 is 170 °C while that of Al-2 wt pct Cu is 107 °C). This gap in the AA7050 database is critical because the semi-solid part of the database is directly linked to the HT susceptibility of the alloy and thus needs to be completed.

The goal of this work was twofold. First, we aimed at completing the ALSIM thermomechanical database in the semi-solid temperature region of an AA7050 alloy. The experimental data required by ALSIM to fit the model include the constitutive tensile mechanical behavior in the semi-solid temperature range, which can be obtained through isothermal tensile tests. The solid fraction range of interest is below the solid fraction (f_s) ~ 0.8[15] (the temperature when mechanical properties of the alloy start to be appreciated, typically described as a rigidity point[25]) down to the nonequilibrium solidus. The tensile mechanical behavior is critical as it is the main mode for HT to happen (the force imposed onto the central part of a billet is in outward radial direction due to the cooling direction in DC casting). Constitutive parameters for the semi-solid ALSIM model were extracted by fitting the model to the obtained experimental tensile curves. The constitutive parameters were obtained by comparing the tensile force-displacement curves from the experimental tensile tests with the results from numerical thermo-mechanical tensile tests that were built using ALSIM. Using this method, we selected the constitutive parameters that provided us with a minimum difference between the numerical and experimental tensile tests.

Second, we aimed at gaining insight into the mechanical behavior of the semi-solid alloy, which was ultimately related to its HT susceptibility. The mechanical behavior of the alloy in the super-solidus regime was quantified through the strength and its ability to accommodate deformation (ductility characteristics) at different solid fractions. Additionally, we were able to estimate the solid fraction where the grain coalescence occurred—suggested by Giraud[26] as the transition point from where the mechanical properties were governed by liquid films into state where mechanical properties were controlled by solid bridges. At this point

the material gains significant strength, thus behaving more like a solid sample tested at a high temperature (*i.e.,* higher strength and able to accommodate more deformation). This transition point is important as it could be considered as the stage where no continuous liquid film remains between the grain boundaries and the alloy is sufficiently ductile to resist the HT formation[21]; therefore, it is an important variable to assess the alloy susceptibility to HT. We also tested the alloy at two different pulling speeds to understand its strain rate sensitivity. Subsequently, the failure mechanism of the tested samples at different solid fractions was elucidated through fracture surface analysis in a scanning electron microscope (SEM). It was reported that in the semi-solid regime there are different mechanical regimes (*i.e.,* brittle and ductile)[6]; hence, it was important to examine this phenomenon in our AA7050 alloy. Furthermore, we also discuss the HT propensity of an AA7050 alloy and compare it to other types of aluminum alloys to gain insight into its HT susceptibility based on the tensile mechanical properties and other thermo-physical properties (*i.e.,* the freezing range and the onset temperature of thermal contraction).

The outcome from this work provides the research community not only with a database which enables better accuracy of ALSIM to simulate DC casting of an AA7050 alloy, but also with insights into the HT susceptibility of this alloy compared to other types of aluminum alloys. This information will ultimately be vital for optimization of AA7050 production.

II. MATERIALS AND METHODS

A. *Experiments*

An AA7050 alloy used in this experiment was produced using the direct-chill (DC) casting method and supplied by Tata Steel Nederland Technology B.V. (IJmuiden). The melt was degassed in the furnace, and a conventional bore mold was utilized during DC casting. The produced billet had a diameter of 315 mm. Optical spectrum analysis was used to determine the chemical composition of the billet (see Table I). The solidification path was simulated through JMAT Pro software shown in Figure 1.

The tensile specimens were cut from the same billet from around mid-radius section parallel to the casting direction without any heat treatment. This assured that the samples had the same chemical composition and microstructure, not affected by macrosegregation. The specimens were tested using a set-up developed at SINTEF Materials and Chemistry with an Instron 5944 series tensile test machine equipped with a 2-kN load cell. The specimen was heated up using an induction heating coil system. The temperature in the center of the specimen was controlled by a calibrated thermocouple connected to a Eurotherm™ temperature controller, which has temperature uncertainty is approximately ± 0.35 °C from the target temperature. The temperatures were measured using thermocouples calibrated against the standard calibrated thermocouple, and the primary values were corrected to the calibrated values so that the estimated uncertainty in the temperature measurements did not exceed 0.8 °C. The thermocouple was positioned in the central mid-length position of the sample, drilled from the edge of the sample in the axial direction of the sample (see Figure 2(a)), and the thermocouple was kept in place by gravity force because we do not want to put extra force onto the semi-solid regime. The schematic of the tensile test setup is shown in Figure 2(a) and the geometry of the tensile specimen in Figure 2(b). The notch near the end of the specimen is designed to reduce the heat flow out of the specimen by the water-cooled surface, thus flattening the temperature gradient across the specimen.

Table I. Average Chemical Composition of AA7050

Elements, Wt Pct								
Zn	Cu	Mg	Zr	Fe	Mn	Si	Ti	Cr
6.15	2.2	2.1	0.13	0.07	0.04	0.04	0.03	< 0.01

A boron-nitride coated quartz-glass tube (coating was only on the inside) was used to enclose the mid-length part of the sample to prevent liquid breakout during the fully liquid phase. The coating was intended to prevent the sticking of the liquid aluminum onto the quartz tube, which may affect the force measurement due to the additional friction resistance. The experimental cycle (for both heating and mechanical testing temperature) is shown in Figure 2(c).

The sample was first heated from room temperature up to T_{max} = 635 °C, which is just above the liquidus of the AA7050 (Figure 1). After that, the samples were held at T_{max} for 60 seconds to ensure that the central mid-length part of the specimen was fully liquid. Then, we cooled down the sample to the test temperature at a cooling rate of 1 °C/s. Subsequently, the sample was kept at the test temperature for approximately 90 seconds to let the temperature across the specimen stabilize. Afterwards, the mechanical deformation was performed with a specified displacement (pulling) rate

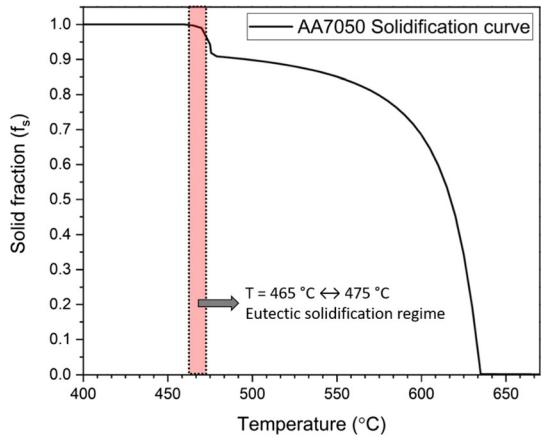

Fig. 1—Solidification path of AA7050 based on JMAT Pro calculation.

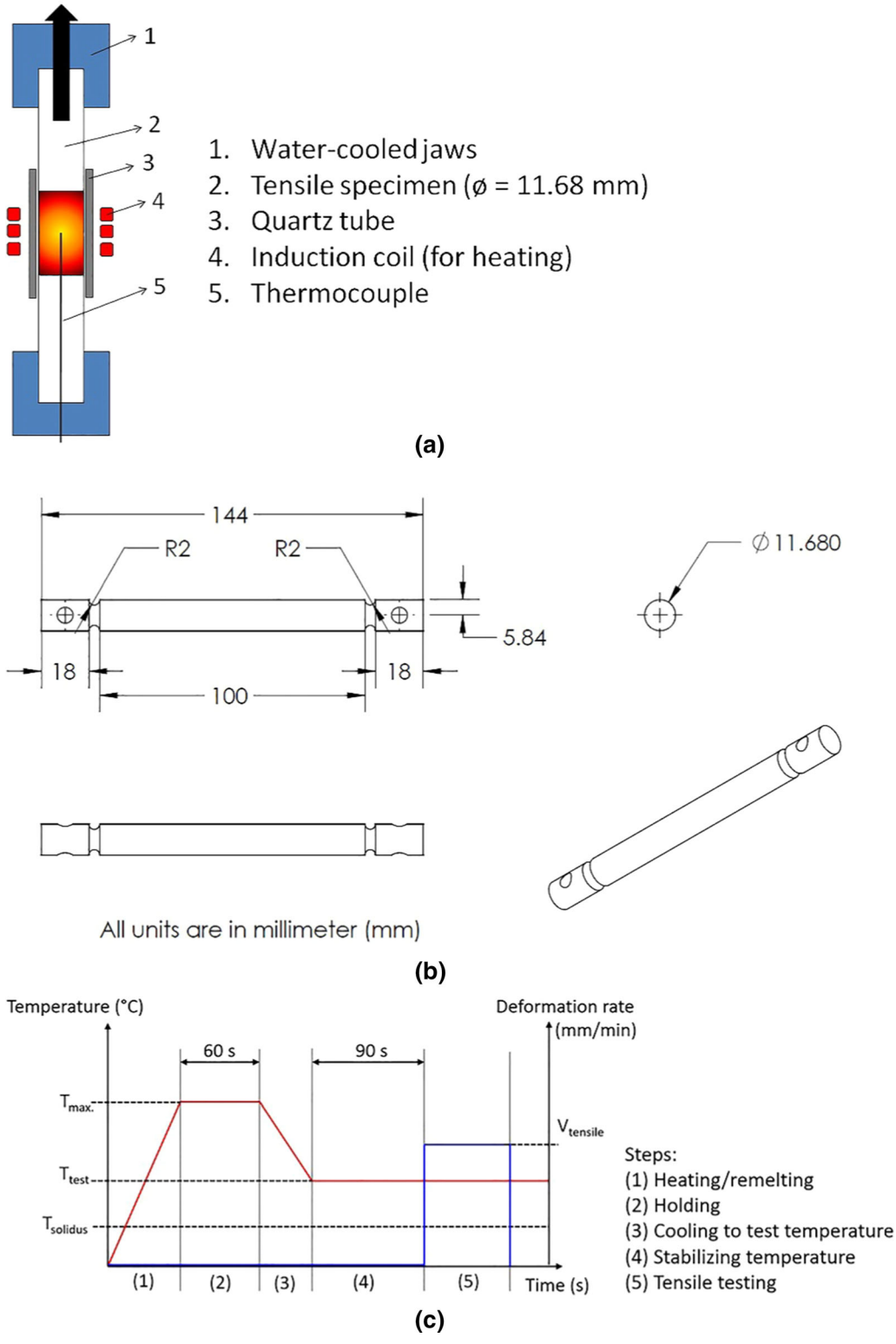

Fig. 2—(*a*) Tensile test setup schematics, (*b*) tensile sample geometry, and (*c*) isothermal tensile test cycle; heating cycle (red line) and mechanical deformation cycle (blue line).

until the force value was approximately zero after the fracture. The accuracy and displacement resolution of the test was 0.003 mm/s (0.2 mm/min).

Two different displacement rates were used (Table II); 0.2 mm/min was chosen to be the lowest displacement rate because at lower rates the liquid parts of the alloy start to stick to the quartz tube and may increase the friction force, thus possibly the measurement error. To study the displacement rate sensitivity of the alloy at this

Table II. Tensile Plan Matrix and the Number of the Tests Performed at Different Test Conditions

Disp. Rate (mm/min)	Test Temp. (°C)						
	465 ($f_s = 1.0$)	470 ($f_s = 0.99$)	473 ($f_s = 0.97$)	475 ($f_s = 0.94$)	485 ($f_s = 0.90$)	520 ($f_s = 0.88$)	550 ($f_s = 0.85$)
0.2 mm/min	3	3	3	3	3	3	3
2.0 mm/min	0	3	0	3	3	0	0

temperature regime, pulling speed with an order of magnitude higher (2 mm/min) was selected.

The test temperatures that we cover in this work correspond to the solid fractions (f_s) in the range where HT typically occurs, *i.e.,* between 0.85 (T = 550 °C), below the rigidity temperature, where the alloy starts to gain mechanical strength, and 1.0 (T = 465 °C), when the alloy is at fully solid state. We carried out tensile tests at different data points, namely at different solid fractions (temperature) and displacement rates as shown in Table II. The solid fraction was correlated with the temperature based on the JMat-Pro® calculation depicted in Figure 1. Three tests were performed to obtain the statistical behavior of the alloy for each combination of temperature and displacement rate. In this work we focus on tensile tests in a low strain rate regime (*i.e.,* between 10^{-3} and 10^{-5} s^{-1}), which is relevant to DC casting.[27] Tests at a higher displacement rate (2 mm/min) were only performed at specific temperature points, which is approximately before and after the typical grain coalescence point in different alloys,[26,28,29] to observe deformation rate sensitivity at different mechanical property regions. Tensile tests were performed until each sample failed. Fracture surface analyses of the failed samples were carried out in a Jeol JSM-6500F scanning electron microscope (SEM).

B. *ALSIM Constitutive Equations*

Mechanical properties of alloys are different at different temperature ranges. There is a dramatic change in the constitutive behavior of alloys in the vicinity of the solidus temperature due to the significant change in morphology (spatial distribution of the remaining liquid phase), strength and ductility of the alloy.[26,30] The semi-solid mechanical behavior of the alloy in ALSIM is described using an advanced viscoplastic constitutive model to represent the coherent part of the semi-solid regime, which allows for the dilatation/densification of the semisolid skeleton under applied deformation. While the full account and detailed explanations of the model could be found elsewhere,[28,31–34] for brevity, in this work we are only focusing on the part of the model that deals with partial cohesion of the mush as shown by Eqs. [1] and [2]. The functions $\alpha(g_s, X)$ and $C^*(g_s, X)$ describe the evolution of the partial cohesion of the mush and must be determined from careful rheological experiments at various fractions of solids and stress states. For grain-refined Al-Cu alloys, Ludwig *et al.*[28] have shown that the following expressions provide a simplified good fit with experimental data. For all stress states (all X values), both functions are described as follows[14,21,28,29]:

$$C^*(g_s, X) = C^*(g_s, X = 0) + \frac{1 - C^*(g_s, X = 0)}{1 + \exp\left[\frac{X_0 - X}{\Delta x}\right]} \quad [1]$$

$$\alpha(g_s, X) = \alpha(g_s, X = 0) \quad [2]$$

where

$$C^*(g_s, X = 0) = \frac{1 - (1 - g_s)^p}{1 + \exp\left(\frac{g_s^{coh} - g_s}{\Delta g_s}\right)} \quad [3]$$

$$\alpha(g_s, X = 0) = \frac{\alpha_0 + \alpha_1 \frac{g_s^{1/3}}{1 - g_s^{1/3}}}{1 + \exp\left(\frac{g_s^{coh} - g_s}{\Delta g_s}\right)} \quad [4]$$

In addition to the $\alpha(g_s, X)$ value for general stress states (X = 0), the most recent version of the model[28,29] includes the option to take into account the effect of coalescence in the tensile stress state, which is the main mode of HT in DC casting, ($X < 0$) through $\alpha(g_s, X)$. The function is described as follows:

$$\alpha(g_s, X < 0) = \frac{\alpha_0 + \alpha_1 \frac{g_s}{1 - g_s} \exp(k(g_s - g_s^{coal})}{1 + \exp\left(\frac{g_s^{coh} - g_s}{\Delta g_s}\right)} \quad [5]$$

where k = 10 and g_s^{coal} = 0.94.[18] When the alloy becomes fully cohesive and reaches the fully solid state (at g_s = 1, C = 1), the alloy becomes ductile and follows the creep law behavior. Therefore, the viscoplastic strain rate tensor could be simplified as follows[21,29]:

$$\dot{\boldsymbol{\varepsilon}}_s^p = \frac{3}{2} \frac{\dot{\varepsilon}_s^p}{\bar{\sigma}_s} \boldsymbol{\tau}_s \quad [6]$$

with

$$\bar{\sigma}_s = \sigma_0 \exp\left(\frac{Q}{nRT}\right) \left(\frac{\dot{\varepsilon}_s^p}{\dot{\varepsilon}_0}\right)^{1/n} \quad [7]$$

This law governs the behavior of the alloy until the merge properties temperature (T_{merge}), which is usually in the vicinity of the solidus temperature (could be up to around 50 °C below solidus). From this point down to onset hardening temperature (T_0), the alloy is governed

Table III. Nomenclature

T	temperature
g_s	volume fraction solid
$\boldsymbol{\tau}_s$	deviatoric part of stress tensor
$\bar{\sigma}_s$	von Mises stress
$\dot{\boldsymbol{\varepsilon}}_s^p$	viscoplastic strain rate tensor
$\dot{\bar{\varepsilon}}_s^p$	effective viscoplastic strain rate
$\bar{\varepsilon}_s^p$	viscoplastic strain
X	stress triaxiality
α, C^*	internal variables function of g_s and X
p, α_0, α_1, X_0, Δx, Δg_s, k	semi-solid parameters of the cohesion model
σ_0, $\dot{\varepsilon}_0$,Q,n	parameters of the high-temperature solid-state creep law
K, r, m	parameters in the extended Ludwik equation (ALSPEN) constitutive model
R	molar gas constant
g_s^{coh}, g_s^{coal}	coherency and coalescence solid fraction, respectively
I	identity tensor

by extended-Ludwik equation or ALSPEN model (Eq. [8]).[35] However, since the hardening effect in this temperature range is not significant, the hardening parameter ($r(T)$) is set to zero. Below T_0, the strain hardening of the alloy starts to become important; thus, $r(T)$ is non-zero. The formulation of the full extended-Ludwik equation used to simulate the mechanical behavior of the alloy at fully solid state is as follows:

$$\sigma = K(T)(\varepsilon_p + \varepsilon_p^0)^{r(T)}(\dot{\varepsilon}_p)^{m(T)} \quad [8]$$

where $K(T)$ is the consistency of the alloy (at $\varepsilon = 1$, $\dot{\varepsilon} = 1$ s^{-1}), $r(T)$ is the hardening parameter, and $m(T)$ is the strain rate sensitivity of the alloy, and the value is inversely proportional to n in Eq. [7]. These parameters are temperature dependent. ε_p^0 is a constant equal to 0.001.[23,35] The constitutive parameters of an AA7050 at sub-solidus temperature were obtained in our previous work.[24] In this work, we set $T_{merge} = 410$ °C and $T_0 = 390$ °C as suggested by Lalpoor *et al.*[23] The nomenclature of each variable in the equations is shown in Table III.

C. *Constitutive Parameters Extraction Procedure*

To describe the semi-solid properties of the alloy, ALSIM uses the constitutive equations described in References 21,28. The internal functions of the semi-solid constitutive equation (Eqs. [1] through [5]) show that the constitutive parameters that need to be extracted and optimized are the rheological parameters p, α_0, α_1, g_s^{coal} and k. Since the parameters of the solid part of the alloy (represented by creep law properties, Eqs. [7] and [8]), *i.e.*, σ_0, $\dot{\varepsilon}_0$, Q and n, were obtained in our previous work,[24] in this study we focus on obtaining the constitutive parameters for the semi-solid part of the constitutive model by utilizing the ALSIM package.

The flow chart of the constitutive parameter extraction procedure is shown in Figure 3. As a prerequisite, two sets of information have to be obtained

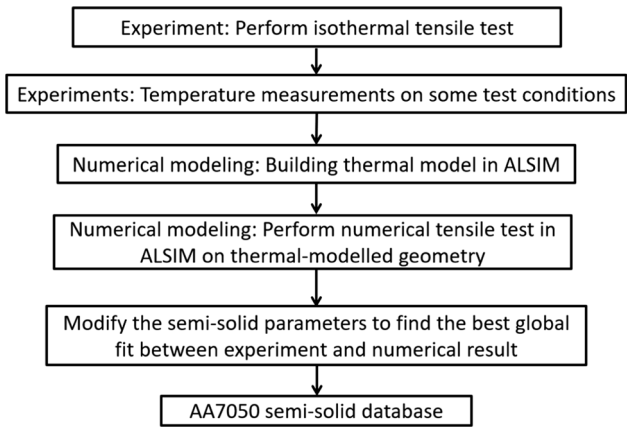

Fig. 3—Flow chart of semi-solid constitutive parameter extraction using ALSIM.

experimentally. The first set of information is the tensile force-displacement curves of the alloy at different solid fractions. The second required set of information is the temperature distribution across the length of the sample at various solid fractions where the isothermal tensile tests mentioned in the previous point have been carried out. After we obtain the necessary information, two steps need to be done to determine the constitutive parameters of the alloy. We start by making a temperature distribution model using ALSIM and verify the simulation results with the experimentally measured temperature. Then, using the sample geometry with modeled temperature distribution, we carry out numerical tensile tests and find the constitutive parameters that have the best fit with respect to the experimental tensile test data (lowest value difference between the numerical and experimental force-displacement curves).

It is necessary to build a temperature distribution model across the sample because the length of the semi-solid regime is different at various test temperatures. In high-temperature mechanical tests, deformation mostly occurs in the weakest part of the sample, *i.e.*,

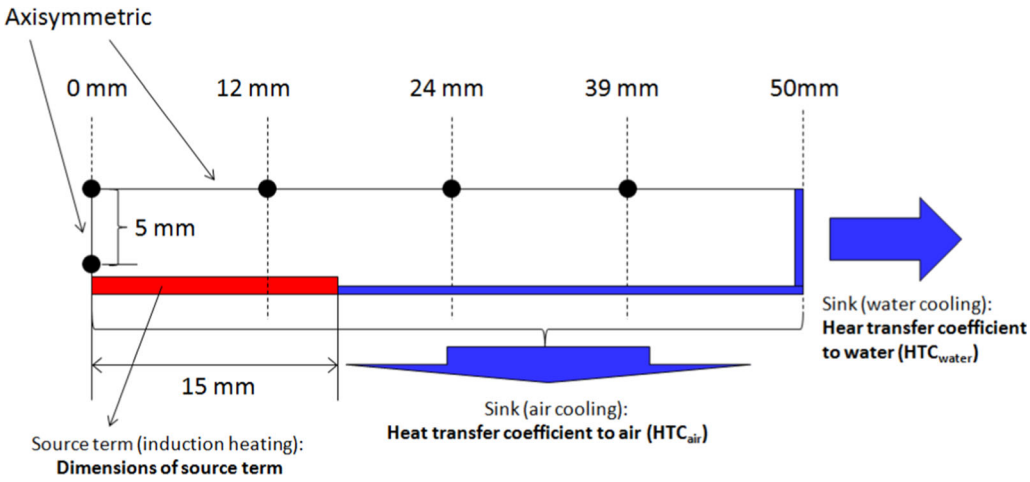

Fig. 4—Thermal model illustration along with model parameters. The black dots represent the temperature measurement points on both the experiment and numerical model.

in this case, at the semi-solid region because this part is significantly weaker compared to the fully solid part.[36,37] Thus, a realistic temperature distribution along the sample is critical for obtaining accurate constitutive parameter values. We built a simple thermal model of the sample using ALSIM, which focuses on the main heat transport phenomena: heating by induction coil and cooling by both a water-cooled surface and air cooling from the ambient temperature. This model aimed at depicting the steady-state temperature distribution along the sample length where the central part of the sample had the test temperature while heat was constantly extracted by the cooling surfaces.

To reduce the calculation time, we made a 2D thermal model by taking an axial cross section of the sample. However, due to axis symmetry and for efficiency, only a quarter of the cross section is simulated. The sample geometry was taken from the gage length of the sample, represented as a sample longitudinal cross section with a length of 50 mm (from the mid-length to just before the notch; see Figure 2) and a width of 5.84 mm. To simulate heat generation, which in the experiment was done by induction heating, a layer of a source term was specified (a specific region in the simulation geometry that injected heat to the system) in the surface area around the mid-length of the sample. The power given by the source term was regulated in such a way that the temperature in the central mid-length of the sample resembled the test temperature. To depict the heat extraction phenomenon, the main heat extraction came from the cooling surface at the end of the sample, and the secondary heat extraction was by the air cooling from the sample surface. The water temperature and ambient room temperature resembled the experimental conditions: water temperature was 8 °C and room temperature 20 °C. The illustration of the thermal model and its parameters is shown in Figure 4. The results obtained with this model were then compared to experimental temperature measurements specifically done for this purpose (no mechanical deformation was performed on the temperature calibration measurements). These tests were done with conditions corresponding to some of the test temperatures specified in Table II. In the experiment, we measured the temperature at four different points—at 0, 12, 24 and 39 mm—off the mid-length along the length of the sample. Additionally, we obtained the radial temperature distribution of the sample by measuring the temperature at the central mid-length and 5 mm off center in the mid-length of the sample. From these measurements, we adjusted the model parameters (dimension of the source term, water heat transfer coefficient or HTC_{water} and heat transfer coefficient to ambient temperature or HTC_{air}) such that a good qualitative fit between the model and the measured temperature was obtained. The obtained parameters are presented in Section III.

After the temperature distribution across the model geometry had been obtained through the numerical model, this a geometry was used as a template for the numerical tensile test at different solid fractions. The numerical tensile test model was also built using ALSIM, which includes a semi-solid mechanical model. The tensile displacement rate used on the simulation is half of its experimental counterpart because the geometry of the simulation is only half the total gage length of the specimen. To describe the solid part of the model (Eqs. [7] and [8]), the parameters obtained in our previous work were used.[24] For the semi-solid part, we used the Al-2 wt pct Cu semi-solid database[28] as an initial guess because of its availability and its similarity to AA7050 in terms of HT susceptibility.[9] Using this combination of databases, we carried out the numerical tensile tests and then compared the value between the numerical and experimental force-displacement results. The aim was to have the minimum difference between these two curves. Thus, we varied the semi-solid constitutive parameters and then executed the numerical tensile tests again until a good qualitative fit was achieved between the numerical test results and their experimental counterparts. However, since the constitutive parameters that need to be fitted are not solid fraction or temperature dependent, a unique set of

parameters (*i.e.*, p, α_0, α_1, g_s^{coal} and k) that yields a reasonable global error for all solid fractions in the semi-solid regime needs to be obtained.

III. RESULTS

A. *Tensile Mechanical Behavior*

Figure 5 shows that the alloy strength increases with solid fraction (decreases with increasing temperature) for both low (0.2 mm/min, Figures 5(a) and (b)) and high (2 mm/min, Figure 5(c)) displacement rates, as have been briefly presented in our previous work.[36] Additionally, from Figures 5(a) and (b) we observe two mechanical property transitions. First, the alloy behavior changes from ductile at $f_s = 1.0$ ($T = 465$ °C) to brittle at $f_s = 0.97$ ($T = 473$ °C). The sharp drop in the ability of the alloy to accommodate deformation and strength at $f_s = 0.97$ ($T = 473$ °C) informs us that the alloy fails in a brittle manner. The second transition in the mechanical behavior of the material occurs when the solid fraction of the alloy decreases from $f_s = 0.97$ ($T = 473$ °C) to $f_s = 0.85$ ($T = 550$ °C). As the solid fraction decreases, the end part of the curve (post-peak part of the curve) changes [*e.g.*, the post-peak slope at $f_s = 0.85$ ($T = 550$ °C) is not as steep as at $f_s = 0.97$ ($T = 473$ °C)], and the slope gradually becomes shallower and starts to have 'tail' after the sharp drop. Finally, at the lowest solid fraction in this test series ($f_s = 0.85$, $T = 550$ °C), the curve resembles a shallow symmetric hump with a long 'tail'. A similar change in the force-displacement curve is also observed at a displacement rate of 2 mm/min (Figure 5(c)). Figure 5(d) shows an example of test repeatability at the lowest solid fraction from the test series: $f_s = 0.85$ ($T = 550$ °C). We can see that the load-displacement curves are generally grouped together especially from the load building phase up to the displacement of 0.3 mm (shortly after the peak force reached) and diverges afterwards. The force value difference between different tests is relatively low (within approximately 5 N). This shows the high quality of the test results despite the presence of a significant liquid fraction in the sample.

Peak force and fracture displacement are used to quantify the mechanical behavior of the alloy. Peak force is described as the maximum force value in the force-displacement curve, and fracture displacement is described as the intersection between the force equals the zero axis and the extrapolation of the last linear regime after the peak force before the sample completely fails. An example of both the peak force and fracture displacement is shown in Figure 5(a).

To relate the peak force value to the strength of the material, as an estimation, the peak force value can be converted into an engineering peak stress by dividing this value with the initial sample cross section. The initial cross section was selected because the sample is relatively brittle especially at solid fractions below solidus; thus, we assumed that the area reduction before fracture is minimum. Figure 6(a) shows that at a

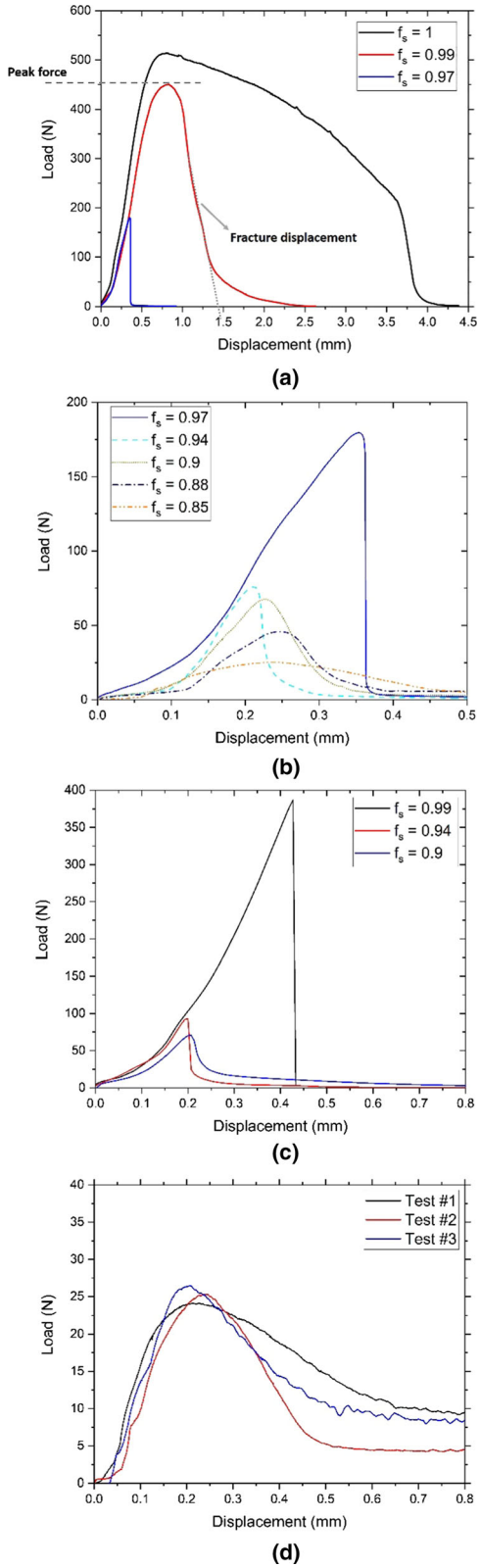

Fig. 5—Force-displacement curves at a low displacement rate (0.2 mm/min) at (*a*) $f_s \geq 0.97$ or $T \leq 473$ °C and at (*b*) $f_s \leq 0.97$ or $T \geq 473$ °C. (*c*) Force-displacement curves at a displacement rate of 2.0 mm/min (adapted from Ref. [36]). (*d*) Example of test repeatability at $f_s = 0.85$ ($T = 550$ °C), with a displacement rate of 0.2 mm/min.

displacement rate of 0.2 mm/min, the minimum engineering peak stress is obtained at $f_s = 0.85$ ($T = 550$ °C) with a value around 0.23 MPa (25 N) while the maximum engineering peak stress is obtained at $f_s = 1.0$ with a value around 4.92 MPa (527 N). There is a significant increase in the peak force as the alloy is cooled down from 475 °C ($f_s = 0.94$) to 473 °C ($f_s = 0.97$). Additionally, for both displacement rates, the peak force rapidly increases as the temperature is lowered below 475 °C ($f_s = 0.94$). One also notices that the alloy starts to become displacement rate sensitive at lower test temperature [starting at 475 °C ($f_s = 0.94$) and below].

Figure 6(b) shows the fracture displacement starts to drop as the test temperature goes above 465 °C ($f_s = 1.0$), and it reaches the lowest point at 475 °C ($f_s = 0.94$) for both displacement rates. The alloy starts to be able to accommodate again at test temperatures above 475 °C ($f_s = 0.94$), forming a well-known U-shaped form (see a review in Reference 6). For both Figures 6a and b, each point in the peak force and fracture displacement represents the average of three tests, and some of the error bars are smaller than the size of the data points.

Figure 6(c) shows the marginal strain rate sensitivity observed either through the force-displacement curve (Figures 5(a) through (c)) or from other mechanical properties between the solid fraction of 0.94 ($T = 475$ °C) and 0.99 ($T = 470$ °C). The main difference in mechanical behavior is that at $f_s = 0.99$ (470 °C), the tests at 2 mm/min resulted in brittle behavior while at 0.2 mm/min some tests showed brittle behavior while other tests showed that the alloy was able to accommodate some deformation (ductile). At 475 °C ($f_s = 0.94$), there is a slight change in the curve shape at different displacement rates with the principal difference found in the post-peak curve shape. At the lower displacement rate, the decrease is more gradual compared to the slope at 2 mm/min.

B. *Fracture Surface Analysis*

SEM fracture surface analysis was performed to reveal the failure mechanisms at different solid fractions. Four samples at different test conditions were observed [*i.e.*, at $T = 470$ °C ($f_s = 0.99$) and $T = 475$ °C ($f_s = 0.94$) and one for each deformation rate], reflecting the transition from brittle to ductile behavior (see Figures 5(a) and (b) and Figures 6(a) and (b)).

The fracture surface analysis informs us that the fracture mode in this semi-solid regime is predominantly inter-granular (dendritic morphology visible at the fracture surface) with some features of the fracture going through the solid bridges between dendrites. Figure 7 shows an example of the fracture surface observed through SEM—the areas within the blue rectangles represent fracture going through the solid bridges while the area within red ellipses reflects the dendritic intergranular fracture mode. Features that possibly attest to broken solid bridges (encircled by dashed red ellipses in Figure 8(a)) were mostly found starting at $f_s = 0.94$ ($T = 475$ °C) and above. At lower solid fractions ($f_s \leq 0.94$ or $T \geq 475$ °C), the broken

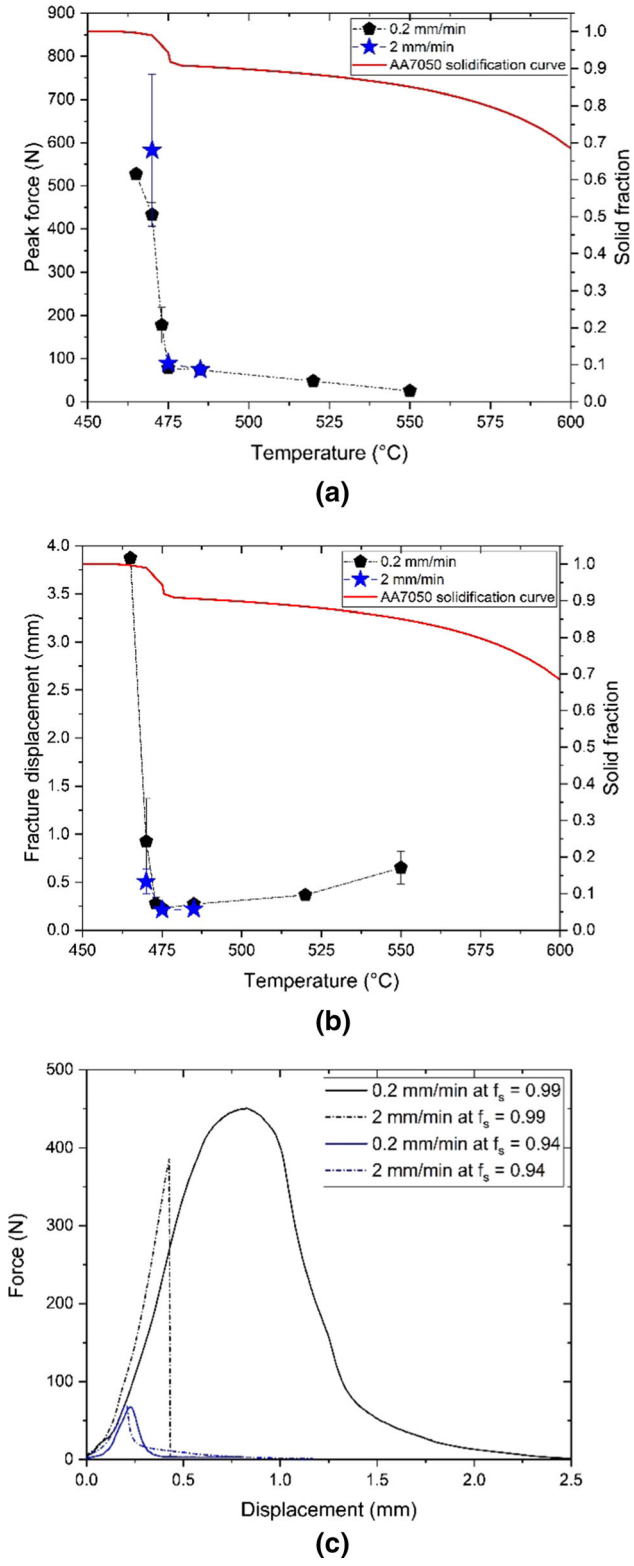

Fig. 6—(*a*) Peak force at different temperatures compared to solid fraction (red line). The temperature measurement uncertainty is within 0.8 °C. (*b*) Fracture displacement at different test temperatures and the comparison with respect to the solid fraction (red line), adapted from Ref. [36]. The error bars in these figures represent standard deviations based on three tests. (*c*) Displacement rate sensitivity at two solid fractions. Before coalescence ($f_s = 0.94$ or $T = 475$ °C) and after coalescence ($f_s = 0.99$ or $T = 470$ °C).

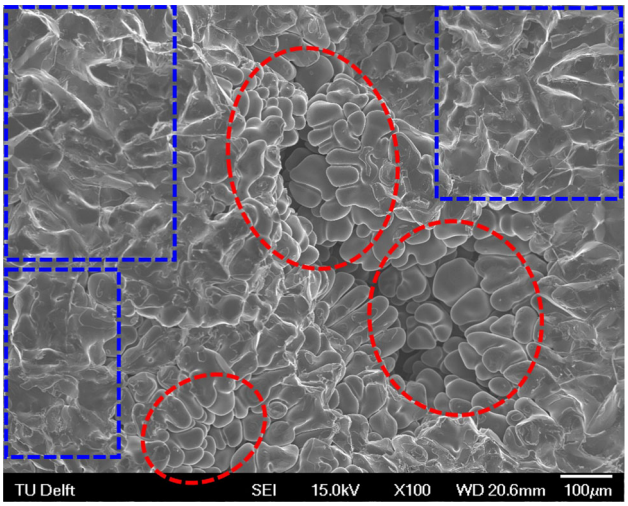

Fig. 7—Typical fracture surface observed in the tensile tested samples in the super-solidus temperature regime—mixed fracture mode. Areas within the dashed blue square represent the fracture going through the solid phase, while the areas within the dashed red ellipses represent the dendritic intergranular features. This SEM picture is taken from the sample tested at $f_s = 0.94$ ($T = 475$ °C) and a displacement rate of 2 mm/min.

interdendritic liquid films (drape-like features within the dashed red ellipses in Figure 8(b)) are commonly observed irrespective of the displacement rate (therefore only fractures at $T = 550$ °C or $f_s = 0.85$, with a displacement rate of 0.2 mm/min, is shown in Figure 8(b)). Note that such interdendritic liquid features are rarely found at the higher solid fractions.

Figure 8(c) shows the common morphology of the solidified interdendritic liquid at the higher solid fraction ($f_s = 0.99$ or $T = 470$ °C) and slow displacement rate (0.2 mm/min). Meanwhile, Figure 8(d) shows the morphology of the solidified interdendritic liquid phase at a similar solid fraction but with a displacement rate of 2 mm/min.

C. *Semi-solid Constitutive Parameter Extraction*

1. *Temperature field comparison*

A good qualitative fit between the thermal model (described in the Materials and Methods section) and the measured temperature was achieved when the following settings were used to run the model: (1) The dimensions of the source term: length of 15 mm and width of 0.6 mm. (2) The heat transfer coefficients to water and air cooling were $HTC_{water} = 1000$ W/m^2 and $HTC_{air} = 10$ W/m^2, respectively. Table IV shows the temperature difference between the measured and modeled temperature ($T_{meas.} - T_{model}$) at different test temperatures along the length of the sample using the mentioned model parameters. From this table, the highest temperature difference between the model and the measurement is found at the test temperature of 485 °C ($f_s = 0.9$) instead of at the extremities of the test temperatures [$T = 550$ °C ($f_s = 0.85$) and $T = 460$ °C ($f_s = 1.0$)].

Figure 9(a) (left) shows the temperature distribution where red corresponds to higher temperatures and blue to lower temperatures while the corresponding solid fraction based on the temperature distribution is shown in Figure 9(a) (right). The result of the model shows that the biggest temperature gradient is along the length of the sample with lower temperature toward the water-cooled surfaces, and there is almost no temperature gradient to the radial direction (approximately 2 °C). This finding is supported by the temperature calibration measurement; the temperature difference between the center and 5 mm off the center of the sample mid-length is approximately 2 °C. This shows a good correlation between the temperature measurement and the model.

The thermal modeling result enables us to estimate the length of the semi-solid region in the sample as shown in Figure 9(b). The semi-solid region is defined as the length between the mid-length of the sample and the solidus point ($f_s = 1.0$ or $T = 465$ °C). The trend shows that the length of the semi-solid regime decreases as the solid fraction increases with a significant drop occurring between $f_s = 0.88$ ($T = 520$ °C) and $f_s = 0.9$ ($T = 470$ °C).

2. *Numerical vs. experimental tensile test*

The numerical tensile test in ALSIM takes place with the geometry that has been temperature modeled as described in the previous section. As the radial temperature distribution was found to be insignificant, for simplicity, in the mechanical part of the simulation we only use the axial temperature distribution along the sample. An example of comparison between the solid fraction and the effective strain distribution in the sample of a numerical tensile test at a solid fraction of 0.9 ($T = 485$ °C) is shown in Figure 10. This figure shows that most of the strain takes place in the semi-solid part of the sample (the region of the sample where the solid fraction is below 1.0 or $T = 465$ °C).

Figure 11(a) shows that the semi-solid constitutive model substantially captures the load development part of the curve. However, the semi-solid parameters are not solid fraction (or temperature) dependent; thus, only a reasonable global minimum error is expected. Examples of a global fit of the semi-solid parameters plotted at different solid fractions and compared to their experimental counterparts are shown in Figure 11(b). This figure illustrates that the results from numerical tests underestimate the experimental forces from $f_s = 0.9$ ($T = 485$ °C) and below, while the results from numerical tests tend to overestimate the experimental forces above $f_s = 0.9$ ($T = 485$ °C).

3. *Constitutive parameters*

From the method shown in the previous section, we obtained semi-solid constitutive parameters for the AA7050 alloy shown in Table V in comparison with those of two other alloys that can be found in references. The result shows AA7050 has the lowest 'p' value while having the highest value of 'α_0' and the value of 'α_1' is between those of the other two alloys.

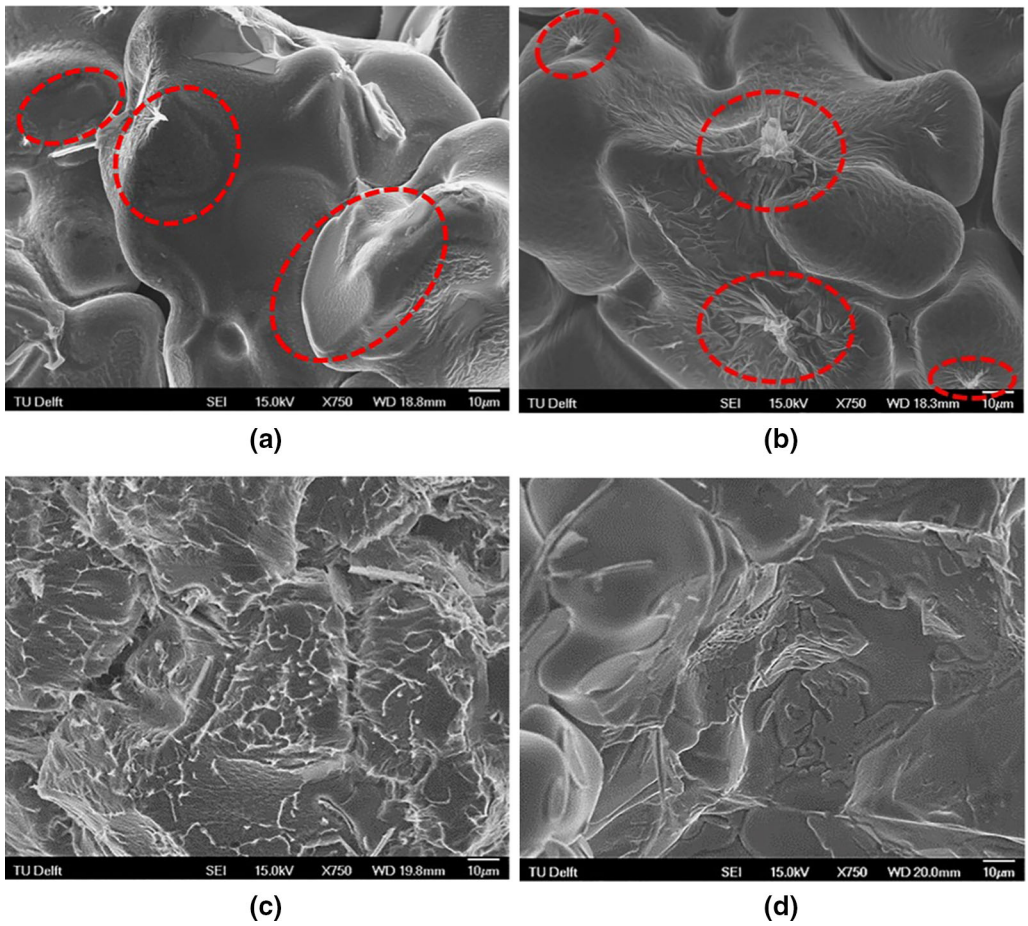

Fig. 8—SEM fracture surface images at higher magnification. (*a*) Broken solid bridges (encircled by dashed red ellipses), commonly observed features starting from $f_s = 0.94$ ($T = 475$ °C) and above. (*b*) Common feature at lower solid fractions ($f_s \leq 0.94$ or $T \geq 475$ °C); broken liquid bridges (drape-like features) encircled by dashed red ellipses. Sample in (a) is tested at 475 °C ($f_s = 0.94$) while in (b) is tested at 550 °C ($f_s = 0.85$), both pulled at a displacement rate of 0.2 mm/min. (*c*) Typical eutectic layer morphology at a higher solid fraction ($f_s = 0.99$ or $T = 470$ °C) with a displacement rate of 0.2 mm/min and (*d*) typical eutectic layer morphology at a higher solid fraction but with a displacement rate of 2 mm/min.

Table IV. Difference Between Measured Temperature ($T_{meas.}$) and Modeled Temperature (T_{model}) in the Axial Length (Center of the Sample) at Different Temperatures in the Mid-Length of the Sample

	Dist. From Center (mm)		
Center Temperature	($T_{meas.} - T_{model}$) 12 mm (°C)	($T_{meas.} - T_{model}$) 24 mm (°C)	($T_{meas.} - T_{model}$) 39 mm (°C)
550 °C ($f_s = 0.85$)	1.4	1.1	− 7
485 °C ($f_s = 0.9$)	− 3.9	− 9.3	− 14.7
473 °C ($f_s = 0.97$)	− 0.6	− 2.5	− 6.5
460 °C ($f_s = 1.0$)	0.4	1.6	− 4.5

To compare the semi-solid constitutive behavior of different alloys in terms of tensile force-displacement curves, we plot the tensile response for each alloy shown in Table V using the numerical tensile test setup in ALSIM (shown in the previous section). Numerical tensile tests were carried out at different solid fractions with deformation speed mimicking the tensile test at the lower displacement rate (0.2 mm/s).

Subsequently, we compared the result of the numerical tensile tests of AA7050 with two different alloys described in Table V, and the outcome is presented in Figure 12. The result shows that in the semi-solid state, AA7050 alloy is stronger than an Al-2 wt pct Cu alloy (Figure 12(a)) but it is weaker that the AA5182 alloy (Figure 12(b)). It is clear that the strength and load development characteristics (the rate of the alloy to reach high force values with respect to displacement) are

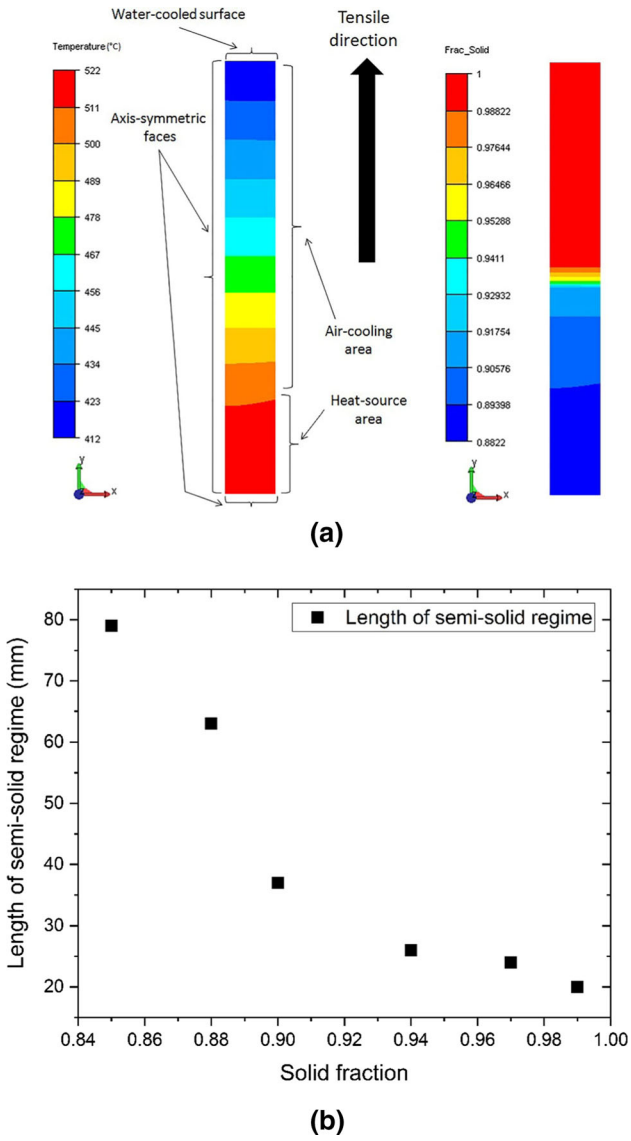

Fig. 9—Example of thermal modeling using ALSIM when the center of the sample is at f_s = 0.88 (T = 520 °C). (*a*) Comparison between temperature (left) and solid fraction (right) distribution. (*b*) Length of the semi-solid regime for the entire gage length of the sample (double the length of the model geometry) for different solid fractions based on thermal model.

dissimilar for the three different alloys. The difference in both strength and behavior becomes more significant as the solid fraction increases, especially starting above f_s = 0.88 (T = 520 °C). In terms of strength, the AA7050 alloy is comparable to the Al-2 wt pct Cu alloy but the load development characteristic is clearly different—AA7050 alloy reaches high force values more quickly than Al-2 wt pct Cu, which has a slower load development mode. In comparison with AA5182, the AA7050 alloy has a relatively similar load development characteristic—a relatively quick increase in load at lower displacement and saturation as the displacement increases. However, it is clear that the semi-solid AA5182 alloy is stronger than the AA7050, especially at higher solid fractions.

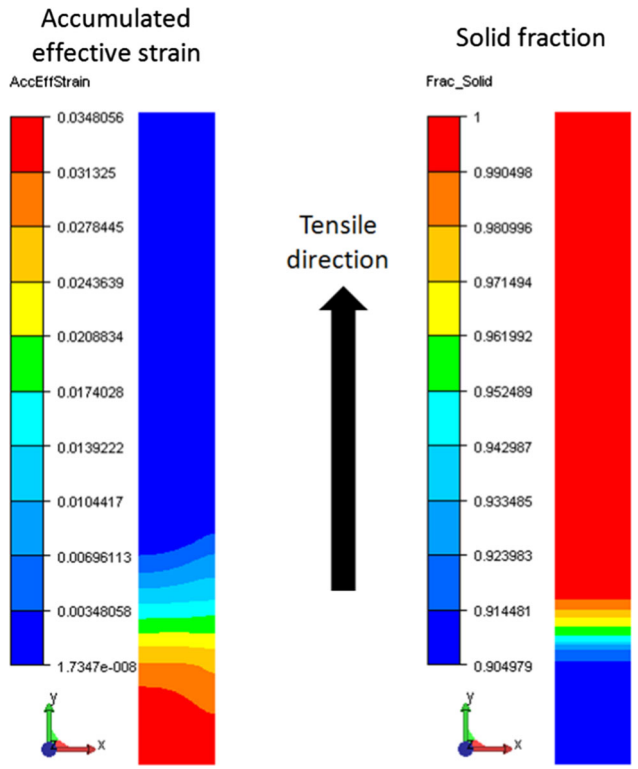

Fig. 10—(Left) Example of the strain calculation result at f_s = 0.9 (T = 485 °C) in comparison to (right) the location of the semi-solid regime based on the solid fraction distribution.

IV. DISCUSSION

A. *Semi-solid Mechanical Properties*

It is well known that the structure affects the semi-solid mechanical properties and HT susceptibility; see, for example, a review in Reference 6. However, the structure parameters such as grain size and dendrite arm spacing become important when their variation is rather strong.[7] Under conditions when the entire sets of samples undergo the same testing procedure (as in our experiments), the differences in structure features are expected to be minimal, like their effect on the properties. In a selection of papers similar in methodology to ours, the structure factor was not taken into account for these reasons, *e.g.* References 38–40, showing that the effect of structure defects is much stronger than the structure parameters such as grain size and dendrite arm spacing. Therefore, we assumed that the structure factor in the mechanical behavior of the samples tested in this work was not influential. The amount of the liquid phase and its distribution had a more decisive effect.

From the evolution of the force-displacement curves at different solid fractions shown in Figures 5(a) through (c), we can deduce the mechanical behavior of the alloy at different solid fractions and relate it to the solidification process. Generally, the evolution of the mechanical behavior is comparable to the solidification process described in previous works[5,6,25,41]; at the beginning of solidification until the coherency temperature, when there is still a significant amount of liquid in

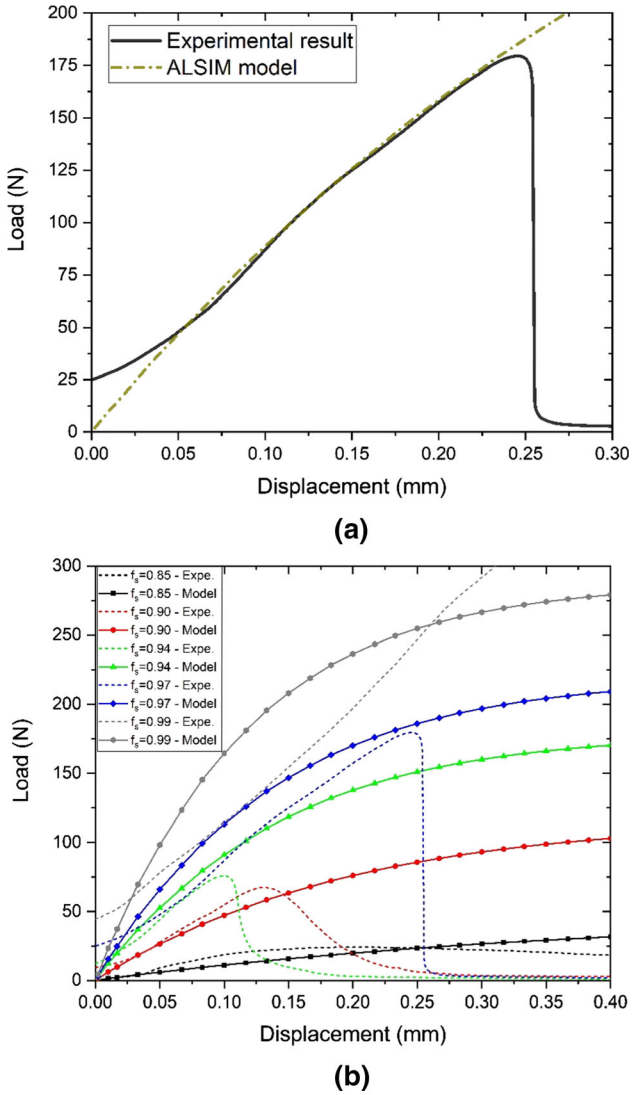

Fig. 11—(*a*) An example of an individual (single-curve fit) comparison between the numerical tensile test (red dash-dotted line) and experimental data (black solid line) at $f_s = 0.97$ ($T = 473$ °C) and a displacement rate of 0.2 mm/min. (*b*) Examples of simultaneous fitting at different solid fractions (global fit).

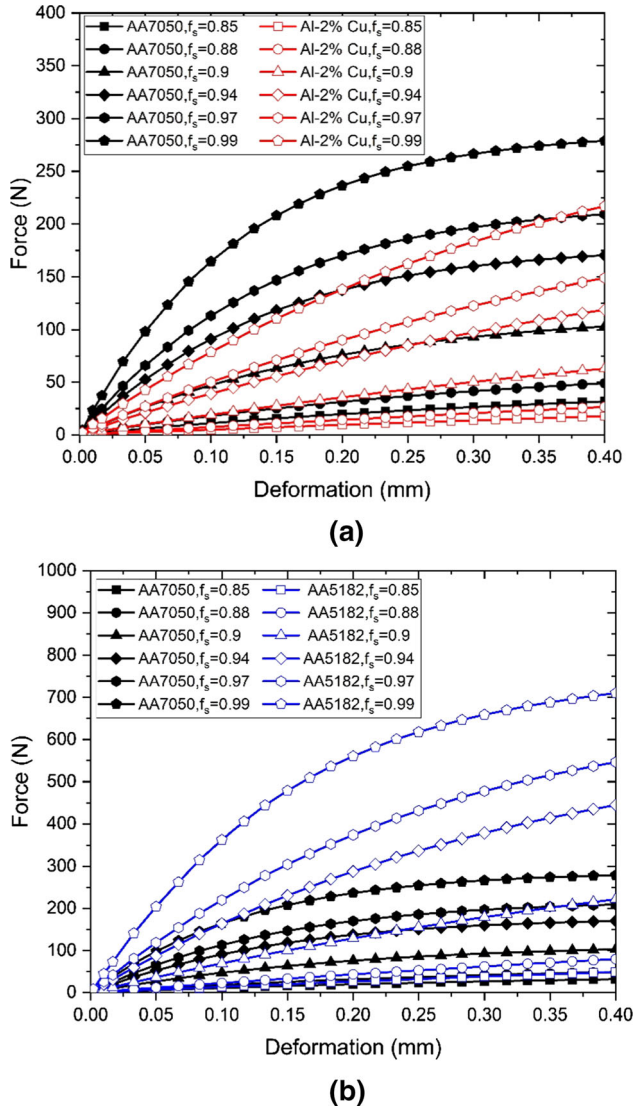

Fig. 12—(*a*) Comparison of modeled tensile response at different solid fractions between Al-2 wt pct Cu (red lines with hollow markers) and AA7050 (black lines with solid markers). (*b*) Comparison of modeled tensile response at different solid fractions between AA5182 (blue lines with hollow markers) and AA7050 (black lines with solid marker lines).

Table V. Comparison of the AA7050 Semi-solid Constitutive Parameters with Those for Different Alloys Described Using the ALSIM Semi-solid Constitutive Equation (Eqs. [3–5])

	Parameters		
Alloys	p	α_0	α_1
AA5182[27,29]	0.315	10.54	0.0632
Al-2 wt pct Cu[28]	0.11	4.45	0.0107
AA7050 (This Work)	0.08	13.65	0.0116

the system, the alloy is fluid, *i.e.,* very "ductile". At a lower temperature, when feeding becomes difficult, the alloy becomes brittle and prone to HT. After the dendrites have merged together, the alloy acquires strength to resist thermal stress, acquiring the ability to accommodate deformation, albeit a very small one. This behavior is commonly observed in various alloys and is described as a brittle or vulnerable temperature range that is linked to the HT susceptibility of the alloy.[6] Moreover, the shape and evolution of the force-displacement curves obtained in this work by tensile testing are similar to those reported on other alloys.[6,27] As the solid fraction decreases, the length of the force 'tail' (after the force-displacement curve reaches the peak force) increases irrespective of displacement rate used for the test. This might be caused by the increasing presence of the liquid phase within the sample during the test. The liquid and some solid bridges between grains continue to hold them together, extending and deforming, creating a fictional elongation despite the fact that the sample is already fractured.[6]

From the result in Figure 6(a), we observe a stark increase in the engineering peak stress from the solid fraction of 0.94 (T = 475 °C) to 0.97 (T = 473 °C), which signifies that the alloy become more resistant to HT formation starting from f_s = 0.94 (T = 475 °C). Meanwhile, Figure 6(b) illustrates the alloy is brittle in the temperature range between solid fractions of 0.9 (T = 485 °C) and 0.97 (T = 473 °C); therefore, the entire test at f_s = 0.94 (T = 475 °C) occurs in the range of the minimum ductility. This also corresponds to the suggestion given in the previous work[26]; liquid feeding stops at approximately f_s = 0.9 (T = 485 °C) but at this solid fraction the grains have not yet coalesced; therefore, the semi-solid material is not yet sufficiently strong to resist developing HT. As the solidification progresses, after passing the most brittle point (at f_s = 0.94 or T = 475 °C), the alloy starts to be able to accommodate deformation again, which could be interpreted as that from this solid fraction on, the microstructure is able to accommodate deformation before HT occurs. This phenomenon resembles the occurrence of grain coalescence as reported elsewhere.[26] This value is supported by other works on different aluminum alloys in which grain coalescence in aluminum alloy typically occurs between f_s = 0.94 (T = 475 °C) and 0.97 (T = 473 °C), such as in AA6060,[41] AA6061,[26] AA6056,[30] Al-1 wt pct Cu,[42] Al-2 wt pct Cu[28] and AA5182.[29]

In terms of deformation rate sensitivity, there were not many differences observed in terms of the force-displacement curve shape (Figure 6(c)), peak force (Figure 6(a)) or fracture displacement Figure 6(b)) for tests conducted with different displacement rates. This may be correlated to the similarities of the fracture surface features at both solid fractions, below (at f_s = 0.94 or T = 475 °C) and above grain coalescence (at f_s = 0.99 or T = 470 °C), as illustrated in Figures 7 and 8. However, the difference in peak stress and fracture displacement at different displacement rates starts to increase with the solid fraction. This might be because at higher solid fractions, there are already more solid bridges connecting the dendrites (*e.g.*, features shown in Figures 7 and 8(a)); thus, the alloy behavior approaches the sub-solidus regime characteristics (presence of positive[38] and increased[24] strain rate sensitivity as the temperature decreases within this temperature regime). Additionally, this condition can also be linked with the increase of error bar width with the solid fraction. This may indicate that at higher solid fractions in the semi-solid range, the alloy strength not only depends on the solid fraction but also on the distribution of the formed damage and/or eutectics at the grain boundaries.

B. *Failure Behavior*

Fracture surface analysis also presents some interesting observations. For instance, the mixed fracture surface features, *e.g.*, dendritic intergranular fracture (within red ellipses in Figure 7) and fracture through the solid phase (within blue squares in Figure 7), were found irrespective of the solid fraction and displacement rate during the test. One possible explanation for this phenomenon is that the dendritic intergranular features are a result of separation of the grains completely covered by the liquid while the fracture can also go through the solid bridges between grains in agreement with HT mechanisms.[5] Therefore, the possible reason for these mixed fracture features observed in our study is because even at the lowest studied solid fraction (f_s = 0.85 or T = 550 °C), the alloy has already transmitted an appreciable load (Figure 5(b)). This means some of the dendrites are already linked together (and able to transmit loads); thus, the separation of dendrites through the solid bridges is possible. Areas within the red ellipse in Figure 8(a) exhibit features that resembles ductile fracture of solid bridges, which is commonly observed at higher solid fractions where grains have welded together.[29] On the lower solid fraction side, *i.e.,* below the coalescence point ($f_s \leq 0.94$ or $T \geq 475$ °C), broken liquid films (drape-like features) develop, as shown in Figure 8(b). Such a morphology is also observed in previous works on semi-solid deformation.[43,44] One possible explanation for the formation of such a feature would be: when there is sufficient liquid phase in the system and mechanical deformation occurs leading to grain separation, the liquid phase clings to the surface of the moving grains held together by surface tension and gradually solidifies, thus leaving spikes and tails. This also explains the lesser prevalence of such a morphology at higher solid fractions, because a sufficient amount of the liquid phase is needed at the grain boundaries to form such drape-like features.

Another interesting fracture surface feature that we observed is that at the high solid fraction (at f_s = 0.99 or T = 470 °C), the morphology of the eutectic is deformation rate dependent (Figures 8(c) and (d)). The tests at a lower displacement rate (0.2 mm/min) show that the former eutectic is more elongated and produces filament-like features. This feature has been also observed in the higher temperature portion of the sub-solidus regime (commonly visible starting at 455 °C[24,37]) at a strain rate of 0.0005 s^{-1}. This could be explained as the micro-superplasticity behavior observed by Takayama *et al.*[45] in an AA7475 alloy near the solidus temperature. The morphology of the micro-superplasticity feature in Figure 8(c) is comparable to the morphology reported at the moderate strain rate given in Takayama *et al.*'s work (2.8×10^{-3} s^{-1}), which is more related to the slower displacement rate (0.2 mm/min) we use in the semi-solid regime tensile test. The whiskers produced in the tests at T = 470 °C (f_s = 0.99) are shorter compared to the tests at 465 °C (f_s = 1.0) at 0.0005 s^{-1}.[24] This can be explained by the trend of superplasticity given in previous works[26,45] in which the length of the filaments is inversely proportional to the pulling speed because if the displacement rate is too high, the viscous flow becomes unstable and the filament cannot form. This may be the reason the length of the filament that we found in this work is relatively short compared to the result by Giraud[26] in the AA6061 alloy at a faster pulling rate. However, another thing that needs to be taken into account is that in terms of chemical composition, AA6061 is quite different from the AA7050 alloy, whereas that difference is less compared to AA7475-type alloys.

C. *ALSIM Numerical Model*

The thermal model that we built using ALSIM shows that the most sensitive parameters influencing the temperature distribution along the axis of the sample are the heat transfer coefficient (to water-cooled surface) and the dimension of the heat source. This is in accordance with the theory since the main thermal influence in the experiment is the heat generated by the heating coil and heat extraction by the water- and air-cooled surface. From the comparison between the temperature calibration measurement and the thermal model in Table IV, we see that the difference is relatively small up to two thermocouples off the mid-length (12 and 24 mm from the mid-length). These two points are considered important because most of the semi-solid regime is formed within this part of the sample especially at the solid fractions important for HT development; above $f_s = 0.9$ ($T = 485$ °C) the length of the semi-solid regime is < 24 mm (Figure 9(b)). The result shows that a simple thermal model could be utilized to perform a constitutive parameter extraction with reasonable quality. Thus, for development of a semi-solid database for other alloys, we may be able to reduce the need to perform temperature calibration measurements at every solid fraction where the tests are carried out (*i.e.,* we only need to do thermal calibration measurements at the highest and the lowest test temperatures), which ultimately saves time and resources. For future development of the thermal model, we suggest increasing the level of realism in the model, for example, by using a temperature (or solid fraction) dependent heat transfer coefficient as it may increase the simulation accuracy.[46]

Figure 11(a) shows that the semi-solid constitutive model in ALSIM can capture the important parts of the force-displacement curve such as the load development part up to the peak force. This figure confirms that a good fit between the experimental and numerical force-displacement curve in an individual fit can be obtained. However, for the global fit (Figure 11(b)), at lower solid fractions ($f_s < 0.94$ or $T > 470$ °C), the simulated force is underestimating the experimental result, while it is the other way around at higher solid fractions. This indicates a compromise in accuracy (from each individual fit) that has to be made to obtain a set of parameters that produce global minimum error. The shapes of the constitutive model curves, however, closely resemble the experimental curve shapes only at certain solid fractions (Figure 11(b)), the shape of the force-displacement curves having reasonable fit below a solid fraction of 0.99 ($T = 470$ °C), where the HT initiation process mainly occurs. These solid fractions [between 0.85 ($T = 550$ °C) and 0.97 ($T = 473$ °C)] are the most critical part for HT formation as in this regime feeding starts to become bad but grains have not yet coalesced; thus, it is important that the model is able to represent this regime accurately. Above the solid fraction of around 0.97 ($T = 473$ °C), the grains typically have coalesced, and thus HT initiation becomes less likely (less liquid is available to serve as initiation points[5,47]); thus, less accurate representation of the experimental tensile profile by the model is acceptable. The global fit quality is comparable to the results obtained for other alloys using similar constitutive equations, such as Al-2 wt pct Cu[28] and AA5182.[29]

The current semi-solid constitutive model in ALSIM is able to reasonably capture the semi-solid behavior of aluminum alloys, especially at the load development phase. However, Figures 5(a) through (c) and also other works on the tensile semi-solid constitutive behavior of aluminum alloys[28,29] show that the damage development phase (the decrease in force value after the peak is reached) is also important because it is directly linked to the propagation of the formed HT. Therefore, an implementation of the damage development model, for instance, the de-cohesion model developed by Mihanyar *et al.*,[48] would be an ideal pathway for further ALSIM model development.

D. *Constitutive Parameters and Hot Tearing Susceptibility*

The result of the semi-solid constitutive parameter extraction in Table V indicates that the AA7050 alloy has distinct parameters and consequently different mechanical behaviors compared to the two other alloys for which the data are available for the ALSIM semi-solid model (*i.e.,* AA5182[27,29] and Al-2 wt pct Cu[28]). The internal variables, C^* (function of p) and α (function of α_0 and α_1), characterize the cohesion rate[21] of the alloy during the solidification process and ultimately can be related to the strength of the alloy. This explains the results of the numerical tensile simulation shown in Figures 12(a) and (b); semi-solid AA7050 is weaker than AA5182 but stronger than Al-2 wt pct Cu. This agrees with other experimental results from other alloys (*i.e.,* for Al-2 wt pct Cu the maximum tensile strength at $f_s = 0.98$ is just above 3 MPa,[28] while for AA5182 at $f_s = 0.96$ it has a maximum tensile strength of almost 7 MPa[29]). As a comparison, the AA7050 in our study has a maximum engineering tensile strength of approximately 5.47 MPa at $f_s = 0.99$ ($T = 470$ °C).

The fact that the AA7050 alloy has lower k values compared to the other aluminum alloys (*i.e.,* AA5182[29] and Al-2 wt pct Cu[28]) shows that for AA7050 (in the tensile stress mode), the strength increase around the grain coalescence point occurs more gradually.

In general, for billet/ingot castings, Al-2 wt pct Cu[28,49,50] and AA7050[23] are known to be susceptible to HT. Based on previous studies,[5,6,12,17,25,51] alloys that are susceptible to HT not only have a wide solidification range, but also have a higher thermal contraction onset temperature (starting at lower solid fractions). Additionally, the tensile mechanical strength in the semi-solid state also seems to be critical as it defines the capability of an alloy to resist HT development. To exemplify this notion, please consider the comparison between Al-2 wt pct Cu and a commercial AA5182. An Al-2 wt pct Cu alloy has a relatively wide solidification range (around 107 °C where the alloy is fully solidified at about 548 °C based on JMAT Pro calculation) and the high thermal contraction onset temperature (starting at approximately at $f_s = 0.9$[51]).

Meanwhile, AA5182 has a wider solidification range (around 185 °C where the alloy reached fully solid state at approximately 450 °C based on JMAT Pro calculation) compared to the Al-2 wt pct Cu alloy, but AA5182 has a lower thermal contraction onset temperature, which corresponds to higher fraction solid (around f_s = 0.95[16]). It is commonly known that Al-Cu alloys are more susceptible to HT than AA5182[51,52].

In comparison, AA7050 has a relatively wide solidification range (approximately 170 °C with fully solid state reached at around 465 °C, Figure 1) but has the lowest fraction solid at the onset of thermal contraction (f_s = 0.83 or at 559 °C[15]); therefore, its vulnerable range (between the onset of thermal contraction and nonequilibrium solidus[6,17,51]) is larger than that of both Al-2 wt pct Cu and AA5182. Additionally, in terms of the semi-solid mechanical strength, at a lower displacement (*i.e.,* strain), where it is relevant to DC casting,[29] AA7050 is weaker than AA5182 although stronger than Al-2 wt pct Cu. From this comparison, we can conclude that AA7050 alloy is severely susceptible to HT; thus, the optimum process parameters to produce sound billets/ingots through DC casting need to be carefully selected.

The results from the ALSIM thermal simulation allow us to approximate the length of the semi-solid regime (Figure 9(b)), where most of the deformation that contributes to HT development occurs. This information combined with the fracture displacement measurement at each solid fraction (Figure 6(b)) can be used to obtain an estimation of the engineering fracture strain, a ratio between fracture displacement and the length of the semi-solid regime at different solid fractions (Figure 13). A potential utilization of this engineering fracture strain data is a HT susceptibility estimation through the comparison with linear contraction data from thermal contraction experiments.[10–12,15,16,51,53] The thermal contraction data may be converted into a strain value. Thus, an experimental-based HT susceptibility measure, such as in the works of Novikov[6,25] and Magnin,[54] could be obtained. The implementation of this criterion in ALSIM would also provide a definitive quantification of whether HT took place during casting, which ALSIM is currently lacking at the moment.

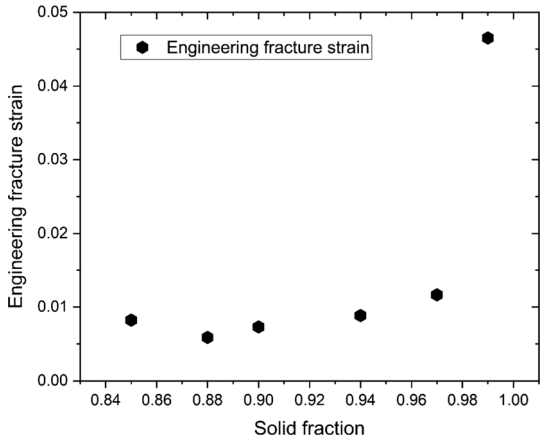

Fig. 13—Engineering fracture strain (strain when fracture occurs) at different solid fractions.

In this work, we demonstrated that a simple thermo-mechanical model built using ALSIM combined with temperature calibration measurements and experimental tensile test data is a reasonable method to extract constitutive parameters for the semi-solid constitutive model (Eqs. [1] through [7]). The results obtained in this work and our previous work in the sub-solidus regime[24] not only completed the database of the AA7050 alloy but also provided an insight into the tensile constitutive behavior, which is necessary for understanding the connection between HT and CC.

The need for a material database sensitivity analysis in the ALSIM model is also supported by our findings in Table V and Figure 12a showing that the AA7050 and Al-2 wt pct Cu alloys have quite different semi-solid mechanical characteristics; thus, we expect differences in the simulation results. Therefore, with the full data set of the AA7050 alloy in the ALSIM materials database, we expect to have better accuracy of thermomechanical and HT simulations upon DC casting. Additionally, the sensitivity of the ALSIM model with respect to different alloys should also been taken into account, as this topic is crucial for ALSIM's long-term development.

V. CONCLUSIONS

In this work, we have performed a detailed study of the tensile constitutive behavior such as strength (through peak force), ability to accommodate deformation (through fracture displacement) and failure mechanisms of the as-cast AA7050 alloy in the semi-solid state. Additionally, semi-solid constitutive parameters of the ALSIM model have been extracted by making a simple thermal model and numerical tensile tests in ALSIM and comparing the simulation result with the experimental mechanical test result. The results and analysis that we obtained in this work can be summarized as follows:

1. From the shape of the force-displacement curves, we found that in the range of f_s = 1.0 (fully solid, T = 465 °C) to f_s = 0.85 (T = 550 °C), the alloy has three different mechanical behavior regimes: ductile at 1.0 (T = 465 °C) ≤ f_s < 0.97 (T = 473 °C), brittle at 0.97 (T = 473 °C) ≤ f_s ≤ 0.9 (T = 485 °C) and then ductile again [at 0.9 (T = 485 °C) < f_s ≤ 0.85 (T = 550 °C)].
2. Grain coalescence for this alloy occurs between f_s = 0.94 (T = 475 °C) and f_s = 0.97 (T = 473 °C), which is signified by the sharp increase in peak force between the mentioned solid fractions.
3. A brittle temperature range fracture displacement curve was observed in the semi-solid regime with the alloy being most brittle at 475 °C (f_s = 0.94), and the alloy gains its ability to accommodate deformation again as the liquid fraction increases in the alloy.
4. SEM fracture surface analysis revealed that in general the fracture mode is mostly intergranular

with fracture propagating through solid bridges as well. Additionally, at higher solid fractions, the morphology of the eutectic is different at different displacement rates (Figures 8(c) and (d)). Features that depicts ductile fracture of solid bridges between grains were observed in samples tested at higher solid fractions (Figure 8(a)), while sites that resemble necking of interdendritic liquid were observed in samples that were tested at lower solid fractions (Figure 8(b)), both independent of the displacement rate used during the test.

5. The semi-solid mechanical behavior of AA7050 is different from the two alloys with the semi-solid database available for ALSIM (*i.e.,* Al-2 wt pct Cu and AA5182). A semi-solid AA7050 alloy is stronger compared to Al-2 wt pct Cu but weaker compared to AA5182.
6. The HT susceptibility of an alloy is not only influenced by the width of the solidification range but also by the mechanical characteristics in the semi-solid state, such as the fraction solid at the onset of thermal contraction, strength and ductility (ability to accommodate deformation). The results from this study suggest that AA7050 is more susceptible to HT compared to Al-2 wt pct Cu and AA5182 because not only does AA7050 have a relatively wide solidification range (170 °C) but also the thermal contraction starts at low fractions of solid (f_s = 0.83 corresponding to 559 °C). Moreover, the semi-solid mechanical strength of AA7050 is lower compared to AA5182.

ACKNOWLEDGMENTS

This research was carried out within the Materials innovation institute (www.m2i.nl) research framework, project number M42.5.09340. The establishment of the experimental set-up and testing procedure for the mechanical tensile testing in the semi-solid has been supported by the Norsk Hydro Fond for SINTEF. The authors express their gratitude to Dr. Démian Ruvalcaba and Mr. Jacob van Oord (Tata Steel Research, Development & Technology, The Netherlands) and also to Mr. Andrew Marson, Mr. Hans I. Lange and Mr. Arne Nordmark (SINTEF Materials and Chemistry, Norway) for their support and inputs. Support from the Modelling assisted INnovation for Aluminum DC Casting process (MINAC) community is highly appreciated.

REFERENCES

1. M. Dixit, R.S. Mishra, and K.K. Sankaran: *Mater. Sci. Eng. A*, 2008, vol. 478, pp. 163–72.
2. E.A. Starke and J.T. Staley: *Prog. Aerosp. Sci.*, 1996, vol. 32, pp. 131–72.
3. D.A. Granger: *Treatise Mater. Sci. Technol.*, 1989, vol. 31, pp. 109–35.
4. N.L. Loh and K.Y. Sia: *J. Mater. Process. Technol.*, 1992, vol. 30, pp. 45–65.
5. D.G. Eskin and L. Katgerman: *Metall. Mater. Trans. A*, 2007, vol. 38A, pp. 1511–19.
6. D.G. Eskin, Suyitno, and L. Katgerman: *Prog. Mater. Sci.*, 2004, vol. 49, pp. 629–711.
7. F. Sheykh-jaberi, S.L. Cockcroft, D.M. Maijer, and A.B. Phillion: *J. Mater. Process. Technol.*, 2019, vol. 266, pp. 37–45.
8. C. Puncreobutr, P.D. Lee, K.M. Kareh, T. Connolley, J.L. Fife, and A.B. Phillion: *Acta Mater.*, 2014, vol. 68, pp. 42–51.
9. Suyitno, V.I. Savran, L. Katgerman, and D.G. Eskin: *Metall. Mater. Trans. A*, 2004, vol. 35A, pp. 3551–61.
10. D.G. Eskin and L. Katgerman: *Mater. Sci. Forum*, 2006, vols. 519–521, pp. 1681–86.
11. A. Stangeland, A. Mo, M. M'Hamdi, D. Viano, and C. Davidson: *Metall. Mater. Trans. A*, 2006, vol. 37A, pp. 705–14.
12. A. Stangeland, A. Mo, Ø. Nielsen, M. M'Hamdi, and D. Eskin: *Metall. Mater. Trans. A*, 2004, vol. 35A, pp. 2903–15.
13. L. Katgerman: *JOM*, 1982, vol. 34, pp. 46–49.
14. M. Lalpoor: Ph.D. Thesis, Delft University of Technology (TU Delft), The Netherlands, 2010.
15. M. Lalpoor, D.G. Eskin, and L. Katgerman: *Int. J. Mater. Res.*, 2011, vol. 102, pp. 1286–93.
16. Suyitno, D.G. Eskin, and L. Katgerman: *Key Eng. Mater.*, 2006, vols. 306–308, pp. 977–82.
17. A. Stangeland, A. Mo, and D. Eskin: *Metall. Mater. Trans. A*, 2006, vol. 37A, pp. 2219–29.
18. T.A.S. Subroto: Ph.D. Thesis, Delft University of Technology (TU Delft), The Netherlands, 2014.
19. D.G. Eskin, V.I. Savran, and L. Katgerman: *Metall. Mater. Trans. A*, 2005, vol. 36A, pp. 1965–76.
20. T. Subroto, A. Miroux, D. Mortensen, M. M'Hamdi, D.G. Eskin, and L. Katgerman: *IOP Conf. Ser.: Mater. Sci. Eng.*, 2012, vol. 33, p. 012068.
21. M. M'Hamdi, A. Mo, and H.G. Fjær: *Metall. Mater. Trans. A*, 2006, vol. 37A, pp. 3069–83.
22. M. Lalpoor, D.G. Eskin, D. Ruvalcaba, H.G. Fjær, A. Ten Cate, N. Ontijt, and L. Katgerman: *Mater. Sci. Eng. A*, 2011, vol. 528, pp. 2831–42.
23. M. Lalpoor, D.G. Eskin, and L. Katgerman: *Metall. Mater. Trans. A*, 2009, vol. 40A, pp. 3304–13.
24. T. Subroto, A. Miroux, D.G. Eskin, and L. Katgerman: *Mater. Sci. Eng. A*, 2017, vol. 679, pp. 28–35.
25. D.G. Eskin: *Physical Metallurgy of Direct Chill Casting of Aluminum Alloys*, CRC Press/Taylor & Francis, Boca Raton, FL, 2008.
26. E. Giraud, M. Suery, and M. Coret: *Metall. Mater. Trans. A*, 2010, vol. 41A, pp. 2257–68.
27. W.M. van Haaften, B. Magnin, W.H. Kool, and L. Katgerman: *Metall. Mater. Trans. A*, 2002, vol. 33A, pp. 1971–80.
28. O. Ludwig, J.-M. Drezet, C.L. Martin, and M. Suéry: *Metall. Mater. Trans. A*, 2005, vol. 36A, pp. 1525–35.
29. O. Ludwig, J.-M. Drezet, P. Ménésès, C.L. Martin, and M. Suéry: *Mater. Sci. Eng. A*, 2005, vols. 413–414, pp. 174–79.
30. D. Fabrègue, A. Deschamps, M. Suéry, and W.J. Poole: *Metall. Mater. Trans. A*, 2006, vol. 37A, pp. 1459–67.
31. O. Ludwig, B. Commet, J.-M. Drezet, C.L. Martin, and M. Suery: in *Proc. MCWASP X, 10th Int. Conf. on Modeling of Casting, Welding and Advanced Solidification Processes*, TMS, Warrendale, PA, 2003, pp. 183–90.
32. O. Ludwig, C.L. Martin, and M. Suéry: *Mater. Forum*, 2004, vol. 28, pp. 357–62.
33. C.L. Martin, M. Braccini, and M. Suéry: *Mater. Sci. Eng. A*, 2002, vol. 325, pp. 292–301.
34. C. Martin, O. Ludwig, and M. Suéry: in *Proc. WCCM V*, *World Congr. on Computational Mechanics V*, Vienna University of Technology, Vienna, 2002.
35. H.G. Fjær and A. Mo: *Metall. Trans. B*, 1990, vol. 21, pp. 1049–61.
36. T. Subroto, A. Miroux, D.G. Eskin, K. Ellingsen, A. Marson, M. M'Hamdi, and L. Katgerman: in *Proc. ICF13, 13th International Conf. on Fracture*, Beijing, China, 2013, pp. 2528–36.
37. T.A.S. Subroto, A.G. Miroux, D.G. Eskin, and L. Katgerman: *IOP Conf. Ser.: Mater. Sci. Eng.*, 2011, vol. 27, p. 012074.
38. A. Alankar and M.A. Wells: *Mater. Sci. Eng. A*, 2010, vol. 527, pp. 7812–20.

39. A.B. Phillion, S. Thompson, S.L. Cockcroft, and M.A. Wells: *Mater. Sci. Eng. A*, 2008, vol. 497, pp. 388–94.
40. G. Chen, F. Lin, S. Yao, F. Han, B. Wei, and Y. Zhang: *J. Alloys Compd.*, 2016, vol. 674, pp. 26–36.
41. L. Sweet, M.A. Easton, J.A. Taylor, J.F. Grandfield, C.J. Davidson, L. Lu, M.J. Couper, and D.H. Stjohn: *Metall. Mater. Trans. A*, 2013, vol. 44A, pp. 5396–5407.
42. V. Mathier, P.-D. Grasso, and M. Rappaz: *Metall. Mater. Trans. A*, 2008, vol. 39A, pp. 1399–1409.
43. I. Farup, J.-M. Drezet, and M. Rappaz: *Acta Mater.*, 2001, vol. 49, pp. 1261–69.
44. M. Rappaz, J.-M. Drezet, P.-D. Grasso, and A. Jacot: in *Proc. MCWASP X, 10th Int. Conf. on Modeling of Casting, Welding and Advanced Solidification Processes*, TMS, Warrendale, PA, 2003, pp. 53–60.
45. Y. Takayama, T. Tozawa, and H. Kato: *Acta Mater.*, 1999, vol. 47, pp. 1263–70.
46. D.C. Weckman and P. Niessen: *Metall. Trans. B*, 1982, vol. 13, pp. 593–602.
47. M. Rappaz, J.-M. Drezet, and M. Gremaud: *Metall. Mater. Trans. A*, 1999, vol. 30A, pp. 449–55.
48. S. Mihanyar, A. Mo, M. M'Hamdi, and K. Ellingsen: *Metall. Mater. Trans. A*, 2011, vol. 42A, pp. 1887–95.
49. J.A. Spittle and A.A. Cushway: *Met. Technol.*, 1983, vol. 10, pp. 6–13.
50. J. Campbell and T.W. Clyne: *Cast Met.*, 1990, vol. 3, pp. 224–26.
51. D.G. Eskin, L. Katgerman, Suyitno, and J.F. Mooney: *Metall. Mater. Trans. A*, 2004, vol. 35A, pp. 1325–35.
52. D. Eskine, J. Zuidema, and L. Katgerman: *Int. J. Cast Met. Res.*, 2002, vol. 14, pp. 217–23.
53. L. Zhang, D.G. Eskin, M. Lalpoor, and L. Katgerman: *Mater. Sci. Eng. A*, 2010, vol. 527, pp. 3264–70.
54. B. Magnin, L. Maenner, L. Katgerman, and S. Engler: *Mater. Sci. Forum*, 1996, vols. 217–222, pp. 1209–14.